Journal of Industrial and Engineering Chemistry xxx (xxxx) xxx

Contents lists available at ScienceDirect

Journal of Industrial and Engineering Chemistry

journal homepage: www.elsevier.com/locate/jiec

Full Length Article

Rational design of porous SnO_2/Fe_xO_y composite microspheres with polydopamine-derived N-doped carbon coating layer as high-performance anode for lithium-ion batteries

Hye Seon Ka [a,1], Geon Hui Oh [a,1], Ji Hun Baek [a], Jae Seob Lee [a,b], Jin-Sung Park [c,d,*], Jung Sang Cho [a,e,f,**]

[a] Department of Engineering Chemistry, Chungbuk National University, Chungbuk 28644, Republic of Korea
[b] Department of Materials Science and Engineering, Korea University, Anam-Dong, Seongbuk-Gu, Seoul 02841, Republic of Korea
[c] Department of Materials Science and Engineering, Ajou University, Suwon 16499, Republic of Korea
[d] Department of Energy Systems Research, Ajou University, Suwon 16499, Republic of Korea
[e] Biomedical Research Institute, Chungbuk National University Hospital, Chungbuk 28644, Republic of Korea
[f] Advanced Energy Research Institute, Chungbuk National University, Cheongju, Chungbuk 28644, Republic of Korea

ARTICLE INFO

Keywords:
Spray pyrolysis
Metal organic framework
Nitrogen-doped carbon
Metal oxide
Lithium-ion batteries

ABSTRACT

Here, the rational design strategy of three-dimensional porous SnO_2/Fe_xO_y microspheres with a conformal N-doped carbon coating as a high-performance anode for lithium-ion batteries is reported. The unique architecture was fabricated via spray pyrolysis using a precursor solution containing Sn-based metal–organic frameworks (MOFs), Fe nitrate, polyvinylpyrrolidone (PVP), and polystyrene (PS) nanobeads, followed by polydopamine (PDA) coating and subsequent carbonization. The resulting microspheres exhibit a continuous mesoporous framework composed of homogeneously dispersed ultrafine SnO_2 and Fe_xO_y nanoparticles, where PS nanobead decomposition generates abundant interconnected pores and Sn-MOF-derived organic framework suppresses particle aggregation. A uniform N-doped carbon layer derived from PDA significantly enhances the electrical conductivity and mechanical stability, facilitating rapid charge transport and effectively mitigating the volume expansion of metal oxides during galvanostatic charge and discharge processes. The microspheres with an optimized amount of N-doped carbon coating layer demonstrate remarkable electrochemical performance, including high reversible capacity, excellent rate capability, and outstanding cycling stability. The microspheres delivered a capacity of 397 mA h g^{-1} after 300 cycles at 5.0 A g^{-1}, which corresponds to the capacity retention of 86 %. In terms of rate capability, a high discharge capacity of 184 mA h g^{-1} was observed even at 10.0 A g^{-1}.

Introduction

The rapid advancement of portable electronics, electric vehicles, and grid-scale energy storage systems has driven an ever-increasing demand for lithium-ion batteries (LIBs) with higher energy density, superior rate capability, and extended cycle life [1,2]. Graphite, despite being the most widely used commercial anode material, possesses a relatively low theoretical capacity (372 mA h g^{-1}), which imposes a fundamental limitation on further performance improvements in next-generation LIBs [3,4]. To address these limitations, transition metal oxides (TMOs) have been extensively investigated as promising alternative anode materials owing to their high theoretical capacities and diverse redox chemistry [5,6]. Among these candidates, SnO_2 has attracted particular attention due to its high theoretical capacity of 1,494 mA h g^{-1} and relatively low operating voltage [7]. However, the practical application of SnO_2-based anodes is significantly hindered by severe volume expansion during lithiation and delithiation, which induces pulverization of active materials, loss of electrical contact, and rapid capacity degradation [8]. Hybridization with other TMOs, such as iron oxides (Fe_xO_y), has been proposed as a viable strategy to mitigate the mechanical instability of SnO_2 and introduce additional electrochemical activity [9,10]. Despite these benefits, both SnO_2 and Fe_xO_y anodes

* Corresponding author at: Department of Materials Science and Engineering, Ajou University, Suwon 16499, Republic of Korea.
** Corresponding author at: Department of Engineering Chemistry, Chungbuk National University, Chungbuk 28644, Republic of Korea.
E-mail addresses: jinsung@ajou.ac.kr (J.-S. Park), jscho@cbnu.ac.kr (J.S. Cho).
[1] These authors contributed equally to this work.

https://doi.org/10.1016/j.jiec.2025.09.004
Received 18 July 2025; Received in revised form 26 August 2025; Accepted 3 September 2025
Available online 12 September 2025

Please cite this article as: Hye Seon Ka et al., *Journal of Industrial and Engineering Chemistry,* https://doi.org/10.1016/j.jiec.2025.09.004

suffer from intrinsic drawbacks, including poor electrical conductivity and substantial mechanical degradation over repeated cycling, which collectively limit their practical viability [11,12].

Recent research efforts have focused on the design of nanostructured composites with engineered porosity and integrated conductive networks [13–15]. Three-dimensional (3D) porous architectures are particularly effective in accommodating volume changes, enhancing lithium-ion transport, and enlarging the electrode–electrolyte interfacial area [16–18]. Additionally, surface modification with conductive carbon layers, especially nitrogen-doped carbon can significantly enhance electrical conductivity and mechanical integrity, enabling stable long-term cycling and enhanced rate performances [19–22]. Among various polymeric precursors for N-doped carbon, such as polypyrrole and polyvinylpyrrolidone (PVP), polydopamine (PDA) offers distinct advantages. Owing to its abundant catechol and amine functional groups, PDA can be spontaneously polymerized under mild aqueous conditions, providing a facile and controllable synthesis route [23]. Additionally, PDA exhibits strong adhesion to diverse substrates, which allows for the formation of uniform and conformal coatings [24]. Upon carbonization, PDA yields N-doped carbon with high nitrogen content and good electrical conductivity, both of which are highly beneficial for improving the electrochemical performance of LIB anodes. Nevertheless, the scalable synthesis of hierarchical porous TMO-based composites, featuring homogeneously distributed active phases and conformal N-doped carbon coatings, remains a significant challenge. Spray pyrolysis, a continuous and scalable technique, has emerged as a promising approach for the fabrication of advanced electrode materials with controlled morphology and tunable composition [25,26].

In this work, we report a rational design and scalable synthesis of three-dimensional porous SnO_2/Fe_xO_y microspheres uniformly coated with N-doped carbon. The synthesis is accomplished via spray pyrolysis using a precursor solution comprising Sn-based metal–organic frameworks (MOFs), Fe nitrate, PVP, and polystyrene (PS) nanobeads, followed by PDA coating and subsequent carbonization. The use of Sn-MOF as a precursor plays a critical role in the formation of ultrafine SnO_2 nanoparticles, which are homogeneously dispersed throughout the porous framework. The decomposition of PS nanobeads during pyrolysis generates a continuous mesoporous structure, while the PDA-derived N-doped carbon coating forms a uniform and conductive shell that enhances the overall electrical conductivity and mechanical stability of the composite. The resulting N-doped carbon coated 3D porous SnO_2/Fe_xO_y microspheres exhibit a highly integrated architecture, which effectively accommodates volume changes, promotes rapid ion and electron transport, and maintains excellent cycling stability. The carefully engineered microspheres maintained a capacity of 397mA h g^{-1} after 300 cycles at a high current density of 5.0 A g^{-1}, corresponding to a remarkable capacity retention of 86 %. Furthermore, microspheres achieved a discharge capacity of 184 mA h g^{-1} at 10.0 A g^{-1}, highlighting their outstanding rate capability.

Experimental section

Synthesis of Sn-MOF

Sn-based metal–organic framework (Sn-MOF) was synthesized as follows. First, Solution A was prepared by dissolving 1.01 g $LiOH{\cdot}H_2O$ (JUNSEI, 95 %) and 1.99 g terephthalic acid (DAEJUNG, 97.0 %) in a mixture of 50 mL DI water and 50 mL N,N-dimethylformamide (DMF, SAMCHUN, Special grade, 99.5 %). Solution B was separately prepared by dissolving 1.13 g $SnCl_2{\cdot}2H_2O$ (ORIENTAL, 95 %) in 20 mL DI water. Solution B was then rapidly added to Solution A under vigorous stirring. After stirring for 60 min at room temperature, the resulting precipitate was collected by centrifugation, subsequently washed with DI water and ethanol, and dried overnight at 60°C.

Preparation of P-SnO_2/Fe_2O_3 microspheres

Half of the total PVP (DAEJUNG, M_w = 40,000; 2 g) was dissolved along with 2.5 g of synthesized Sn-MOF in 200 mL DI water and dispersed overnight using a probe ultrasonicator. After overnight sonication, the remaining half of PVP (2 g), 12.3 g Fe nitrate nonahydrate ($Fe(NO_3)_3{\cdot}9H_2O$, KANTO, 98.5 %), and 200 mL of PS nanobeads solution (particle size ~ 100 nm) were added. The mixture was stirred continuously for 6 h. The homogeneous precursor solution was subjected to spray pyrolysis at 700°C in air, with an air flow rate of 10 L min^{-1}, which resulted in the formation of P-SnO_2/Fe_2O_3 microspheres. For preparing the comparison sample (F-SnO_2/Fe_xO_y without PS nanobeads), an identical procedure was carried out, excluding the addition of PS nanobeads.

Preparation of P-SnO_2/Fe_xO_y@PDA10 microspheres

For PDA coating, 0.12 g of tris buffer (Sigma-Aldrich, ≥99 %) was dissolved in 100 mL DI water, followed by the addition of 0.1 g spray-pyrolyzed powder under stirring. Subsequently, 1.0 g dopamine hydrochloride (Sigma-Aldrich, ≥98 %) was added, and the mixture was stirred for 16 h at room temperature. The resulting coated powder was collected by centrifugation at 8000 rpm for 20 min, washed three times with DI water, and dried at 60 °C. Subsequently, the composite was subjected to heat treatment at 400 °C for 3 h under a N_2 atmosphere for carbonization purpose.

Materials characterization

The structural and physicochemical properties of the synthesized microspheres, namely P-SnO_2/Fe_xO_y@PDA10, P-SnO_2/Fe_2O_3, and F-SnO_2/Fe_xO_y, were comprehensively investigated using various analytical techniques. Crystal phase identification was performed via X-ray diffraction (XRD, Malvern Panalytical, Cu Kα radiation, λ = 1.5418 Å) at the Korea Basic Science Institute (Daegu). Surface morphology and microstructural features were examined using field-emission scanning electron microscopy (FE-SEM, Hitachi S-4500) and field-emission transmission electron microscopy (FE-TEM, JEM-2100F, JEOL). Thermogravimetric analysis (TGA) was conducted in air from 30 to 600 °C at a heating rate of 10 °C min^{-1} to assess compositional stability. Chemical bonding and elemental states were probed by X-ray photoelectron spectroscopy (XPS, K-Alpha, Thermo Scientific, Al Kα source) at the Korea Basic Science Institute (Busan). Nitrogen adsorption–desorption isotherms were collected to determine the specific surface area and pore size distribution, with data analysis based on the Brunauer–Emmett–Teller (BET) method. The carbon and nitrogen contents were quantified by elemental analysis (EA). Raman spectroscopy (RAMANtouch, Nanophoton) was employed to evaluate the crystallinity of the carbonaceous species. The elemental composition ratios were further verified by inductively coupled plasma optical emission spectroscopy (ICP-OES, Spectro ARCOS).

Electrochemical measurements

Electrochemical performance of the prepared microspheres was evaluated using 2032-type coin cells. Working electrodes were prepared by blending active material, Super-P conductive carbon, and sodium carboxymethyl cellulose (CMC) binder in a mass ratio of 7:2:1, followed by casting the resulting slurry onto copper foil. The coated electrodes were dried at 60 °C overnight, then punched into 14 mm diameter disks with an average active material loading of ~ 0.7 mg cm^{-2} (total active mass ≈ 1.0 mg). All cell assembly steps were conducted in an argon-filled glovebox to minimize moisture and oxygen exposure. Lithium metal and microporous polypropylene film served as the counter electrode and separator, respectively. The electrolyte consisted of 1 M $LiPF_6$ dissolved in a 1:1 vol ratio mixture of fluoroethylene carbonate (FEC)

and dimethyl carbonate (DMC). Galvanostatic charge–discharge cycling was performed over a voltage range of 0.001–3.0 V (vs. Li/Li^+) at various current densities (0.1–10 A g^{-1}) using a WBCS3000 battery cycler (WonATech). Cyclic voltammetry (CV) was carried out at a scan rate of 0.1 mV s^{-1}. Electrochemical impedance spectroscopy (EIS) was recorded in the frequency range of 100 kHz to 0.01 Hz with an amplitude of 10 mV.

Results and discussion

PDA-derived N-doped carbon coated porous SnO_2/Fe_xO_y microspheres (P-SnO_2/Fe_xO_y@PDA microspheres), featuring a porous framework composed of SnO_2 derived from Sn-MOF and Fe_xO_y, were synthesized through spray pyrolysis and PDA coating (Scheme 1). The colloidal precursor solution consisting of Sn-MOF, Fe nitrate, PVP, and PS nanobeads (ϕ = 100 nm) was atomized into fine droplets using an ultrasonic nebulizer (Scheme 1-①). Sn-MOF and Fe nitrate were used as Sn and Fe precursors, respectively, while PVP and PS nanobeads served as sacrificial carbon precursors and porogen. The generated droplets were transported by air through the vertical quartz reactor tube at 700 °C, leading to the crystallization of SnO_2 and Fe_2O_3 and the decomposition of PS nanobeads and PVP. In particular, during SnO_2 crystallization, the organic framework in Sn-MOF effectively prevented the aggregation of SnO_2, thereby promoting the formation of smaller nanoparticles. The decomposition of PS nanobeads generated pores, forming the continuous mesoporous framework throughout the microsphere. PVP was introduced as a sacrificial additive to enhance the dispersion stability of precursors and suppress particle aggregation during spray pyrolysis. Through the spray pyrolysis process, porous microspheres consisting of SnO_2 and Fe_2O_3 nanoparticles (P-SnO_2/Fe_2O_3 microspheres) were successfully collected from the bag filter (Scheme 1-②). P-SnO_2/Fe_2O_3 microspheres treated with PDA were carbonized at 400 °C in N_2 atmosphere, which formed the uniform N-doped carbon coating on the surface (Scheme 1-③). The PDA-derived N-doped carbon layer significantly enhances electrical conductivity, facilitating faster electron and lithium-ion transport. Additionally, this carbon layer effectively suppresses the volume expansion of SnO_2 and iron oxides during charge/discharge process, improving structural stability and cycling performance. During the carbon coating process, partial reduction of Fe_2O_3 to Fe_3O_4 was observed. This reduction is primarily attributed to the carbothermal reduction effect, wherein the carbonaceous species derived from the thermal decomposition of polydopamine act as a reducing agent for Fe_2O_3 [27,28]. In an oxygen-deficient (N_2) environment, carbon originating from the polydopamine coating reacts with Fe_2O_3, removing oxygen and thereby facilitating its conversion to Fe_3O_4. Even after the coating process, the porous structure is well-maintained, allowing smooth electrolyte penetration and expanding the active surface area for efficient redox reactions. The interconnected pores also shorten lithium-ion diffusion pathways, enabling faster ion transport and improving reaction kinetics.

The comprehensive analysis was conducted to characterize the nanostructures obtained at various stages of the synthesis and to elucidate the formation mechanism. The FE-SEM image and XRD pattern of Sn-MOF used in this study are presented in Fig. S1, where the average size of Sn-MOF particles calculated from the FE-SEM image is 44.5 nm. The morphological, crystallographic, and elemental mapping analyses for P-SnO_2/Fe_2O_3 microspheres, which are collected directly from the one-pot spray pyrolysis of a precursor solution that contains Sn-MOF, Fe

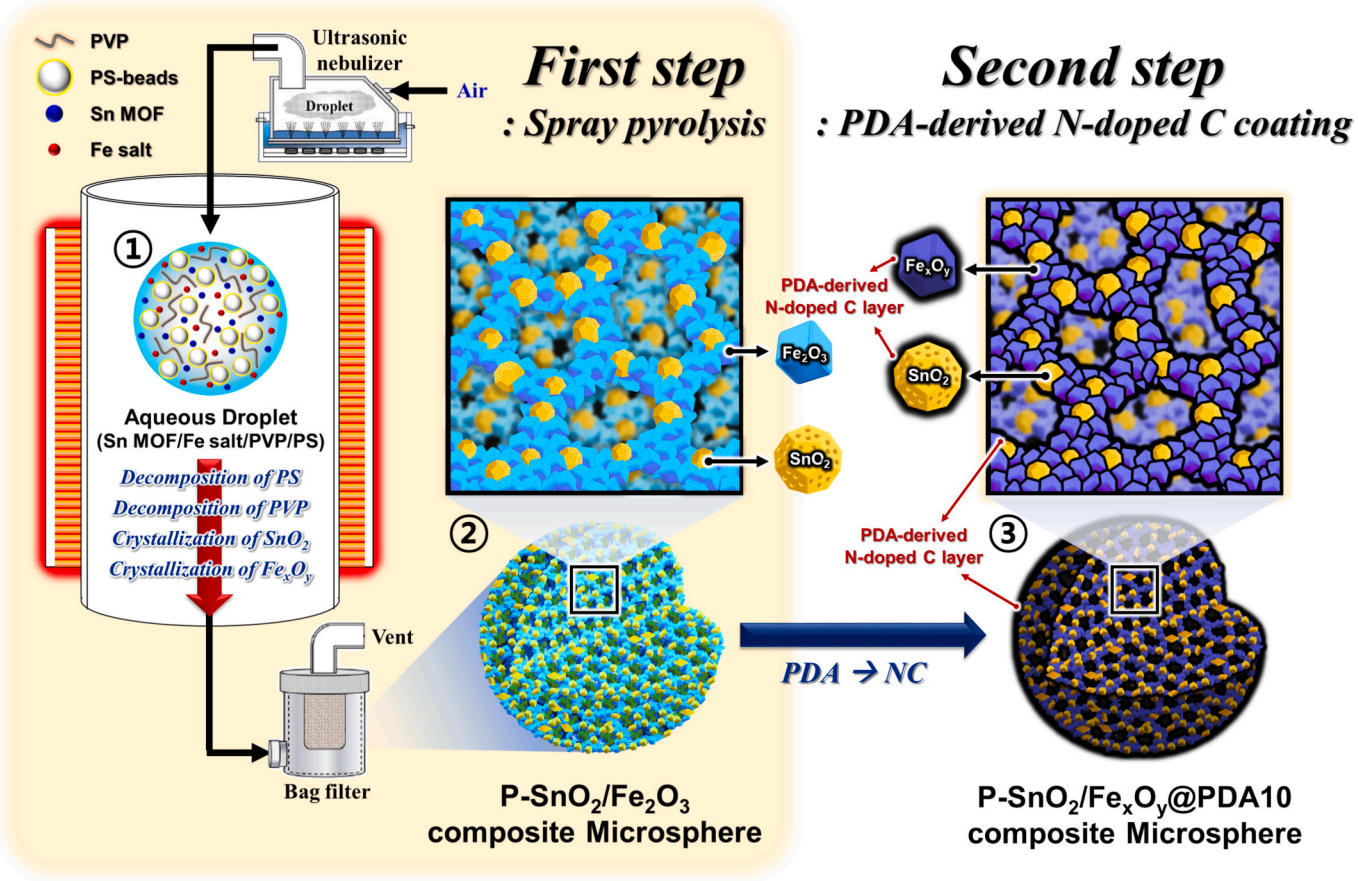

Scheme 1. Schematic representation (①–③) of the formation mechanism of porous SnO_2/Fe_xO_y composite microsphere with polydopamine-derived N-doped carbon coating layer (P-SnO_2/Fe_xO_y@PDA10).

nitrate, PVP, and PS nanobeads, are presented in Fig. 1. Microspheres exhibited porous structures with an average pore size of approximately 50 nm (Fig. 1a and b). These pores originated from the removal of PS nanobeads (initially 100 nm in diameter) during spray pyrolysis, and the pore size reduction to 50 nm is attributed to the microsphere shrinkage during the thermal process. As shown in the fractured cross-section, the pores are uniformly present on the surface as well as inside the spheres (Fig. 1c). The TEM images in Fig. 1d and e confirm the presence of microspheres with uniformly distributed pores, consistent with the FE-SEM results. In Fig. 1e, the bright regions correspond to open pores, while the dark regions represent the framework composed of SnO_2 and Fe_2O_3 nanoparticles. As shown in Fig. 1f, the TEM image illustrates the porous framework composed Fe_2O_3 and ultrafine SnO_2 nanoparticles. This is corroborated by the HR-TEM image in Fig. 1g, which reveals the (110) lattice planes of SnO_2 with the spacing of 0.34 nm and the (104) lattice planes of Fe_2O_3 with the spacing of 0.27 nm. The selected area electron diffraction (SAED) pattern in Fig. 1h distinctly displays diffraction rings corresponding to SnO_2 and Fe_2O_3. The XRD results shown in Fig. 1i further confirm that the microspheres are composed of SnO_2 and Fe_2O_3 phases. The average size of SnO_2 and Fe_2O_3 particles calculated from the Scherrer equation were 14.1 and 3.2 nm, respectively, consistent with the TEM results shown in Fig. 1f. Elemental mapping in Fig. 1j confirms that Sn, Fe, O, C, and N are evenly distributed across the structural framework. The faint C and N mapping indicates that the spray pyrolysis process in an air atmosphere resulted in negligible carbon content, consistent with the EA and TG results shown in Fig. S2. Based on the EA analysis in Fig. S2a, the P-SnO_2/Fe_2O_3 microspheres are composed of 0.4 wt% carbon and 0.9 wt% nitrogen. Supporting this observation, the TG results obtained under an air atmosphere indicate that the slight weight loss is attributed to moisture evaporation and the combustion of a small amount of carbon present in the microspheres (Fig. S2b).

To enhance electrochemical performance, P-SnO_2/Fe_2O_3 microspheres were coated with PDA-derived N-doped carbon (Fig. 2), where the optimum amount of PDA for coating was determined by controlling the weight of PDA added to P-SnO_2/Fe_2O_3 microspheres. The coating was carried out by mixing 0.1 g of P-SnO_2/Fe_2O_3 microspheres with 0.5, 1.0, and 2.0 g of PDA (referred to as PDA5, PDA10, and PDA20, respectively) followed by heat treatment at 400 °C under a nitrogen atmosphere. N-doped carbon coating offers advantages including improved electrical conductivity and structural stability, as well as suppression of active material volume expansion, thereby enhancing electrochemical performance. Fig. 2a–d show FE-SEM images of the composite microspheres according to the PDA coating amount, demonstrating the blockage of surface pores with increasing carbon content. As confirmed by EA analysis, the carbon contents in

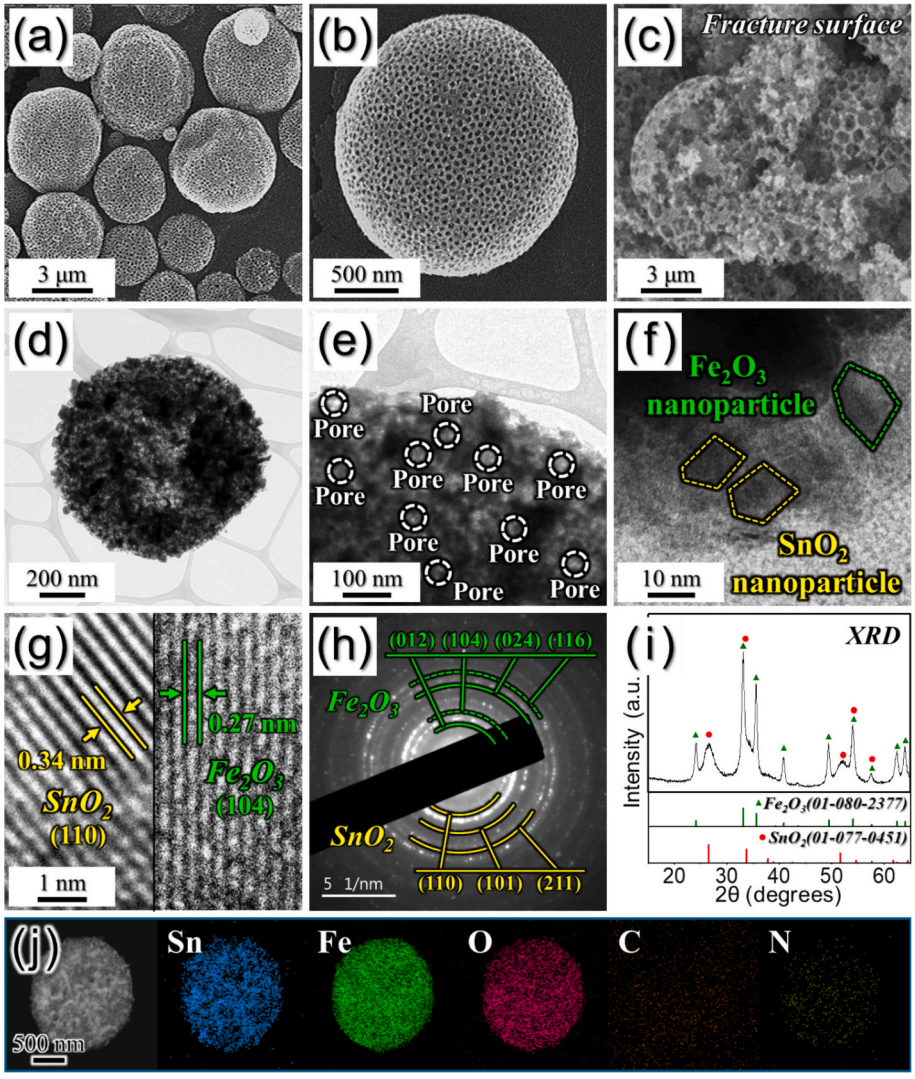

Fig. 1. Physical characterizations of P-SnO_2/Fe_2O_3 microspheres prepared by spray pyrolysis: (a–c) FE-SEM images, (d–f) TEM images, (g) HR-TEM images, (h) SAED pattern, (i) XRD pattern, and (j) elemental mapping images.

microspheres mixed with PDA amounts of 0.5, 1.0, and 2.0 g are 24.1, 30.1, and 36.1 wt%, respectively, indicating an increase in carbon content at higher PDA amount (Table S1). Additionally, at higher PDA coating amount, the amount of nitrogen increased, reaching 5 wt% when PDA amount of 2.0 g was used; the nitrogen-rich PDA can facilitate the formation of an electrically conductive nitrogen-doped carbon matrix. Electrochemical performance according to coating amounts was evaluated by testing the cycle performance at current densities of 0.5 and 1.0 A g^{-1}, as shown in Fig. 2e and f. Prior to evaluating cycling performance at 0.5 and 1.0 A g^{-1}, an activation step was performed for two cycles at 0.1/0.2/0.5 A g^{-1}, respectively. The capacities of P-SnO_2/Fe_xO_y microspheres composited with N-doped carbon initially increased with the amount of PDA coating, peaking at a content of 10 times. This enhanced performance resulted from the development of a three-dimensional conductive carbon network derived from PDA. However, when the PDA content was increased to 20 times, the capacity decreased rapidly, reflecting the inherently lower specific capacity of excessive carbon content. P-SnO_2/Fe_2O_3 microspheres without carbon coating showed rapid deterioration of cycling stability since the fragile pore-wall structure is susceptible to structural degradation during repeated lithiation/delithiation cycles. PDA-derived N-doped carbon coated microspheres exhibited superior capacity retention over repeated cycles compared to the pristine microspheres without carbon coating, clearly highlighting the benefits of the conductive and mechanically robust carbon matrix. This enhancement is attributed to the effective suppression of structural degradation caused by repeated lithiation/delithiation cycles, reinforcing structural integrity. In addition to cycling performance, Fig. 2g illustrates the rate capability test results according to coating amount. P-SnO_2/Fe_xO_y microspheres with PDA 1.0 g exhibited the highest rate performance, where capacities of 1206, 1054, 955, 850, 787, 715, 558, 470, 360, 276, and 184 mA h g^{-1} were obtained at 0.1, 0.2, 0.3, 0.5, 0.7, 1.0, 2.0, 3.0, 5.0, 7.0, and 10.0 A g^{-1}, respectively. Since the 3D continuous conductive carbon matrix was formed on the surface of P-SnO_2/Fe_xO_y microspheres, the microspheres with 0.5 g and 2.0 g carbon coating also exhibited high rate performance. Similar to the cycling performance evaluation, microspheres with PDA 1.0 g demonstrated the best rate capability. P-SnO_2/Fe_xO_y@PDA10 microspheres likely achieved optimal balance, improving electrical conductivity and effectively suppressing active material volume expansion.

Fig. 3 presents comprehensive morphological, structural, and compositional analyses of P-SnO_2/Fe_xO_y@PDA10 microsphere. FE-SEM images (Fig. 3a–c) demonstrate the spherical morphology with

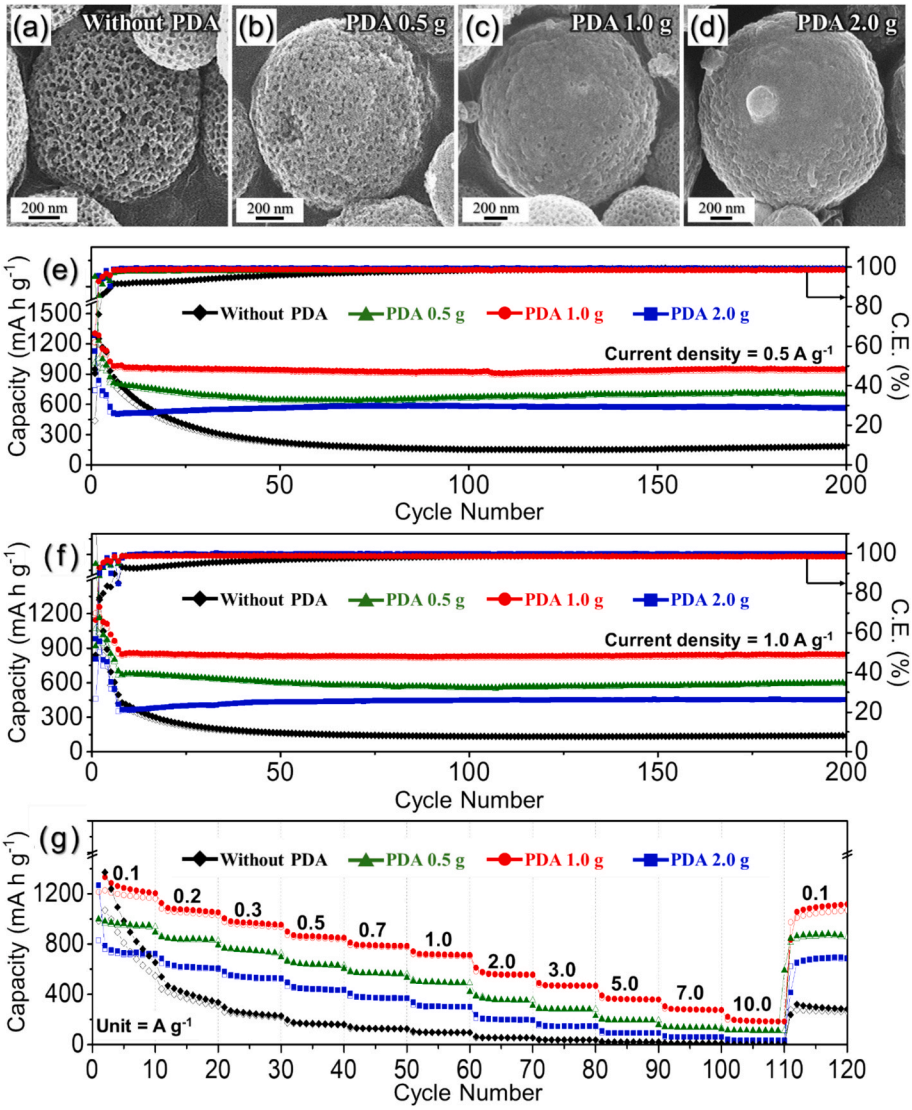

Fig. 2. (a–d) FE-SEM images and (e–g) electrochemical properties of P-SnO_2/Fe_xO_y@PDA microspheres synthesized with different amounts of dopamine hydrochloride: (a) Without PDA, (b) PDA 0.5 g, (c) PDA 1.0 g, (d) PDA 2.0 g, (e) cycling performances at current density of 0.5 A g^{-1}, (f) cycling performances at current density of 1.0 A g^{-1}, and (g) rate performances.

diameters predominantly in the micron range and a porous surface, as observed in the magnified view (Fig. 3b). The fracture surface (Fig. 3c) clearly reveals the internal porous framework, suggesting effective pore generation during synthesis due to the decomposition of PS nanobeads. TEM analysis further confirms the highly porous structure with uniformly dispersed nanopores (Fig. 3d). A distinct PDA-derived N-doped carbon layer uniformly coats the surface, as revealed by TEM imaging (Fig. 3e and Fig. S3), which clearly distinguishes the PDA-coated P-SnO_2/Fe_xO_y@PDA10 microspheres from the uncoated P-SnO_2/Fe_2O_3 counterparts, thereby providing structural integrity and enhancing electrical conductivity. Notably, ultrafine Fe_2O_3 and SnO_2 nanoparticles with sizes less than 5 nm could be observed (Fig. 3f); The SnO_2 nanoparticles originated from the Sn-based MOF precursor, while the Fe_xO_y nanoparticles formed through nucleation and growth of Fe_3O_4, generated via partial reduction of Fe_2O_3 during N_2 annealing. The polydopamine coating effectively suppressed grain growth, leading to the formation of ultrafine Fe_xO_y particles. HR-TEM images (Fig. 3g) show clear lattice fringes separated by 0.34, 0.27, and 0.25 nm, corresponding to the (1 1 0) plane of SnO_2, (104) plane of Fe_2O_3, and (103) plane of Fe_3O_4, respectively. SAED patterns in Fig. 3h further corroborate the polycrystalline nature, displaying characteristic diffraction rings attributed to SnO_2, Fe_2O_3, and Fe_3O_4 phases. This is in line with the XRD pattern of P-SnO_2/Fe_xO_y@PDA10 microspheres in Fig. 3i. P-SnO_2/Fe_xO_y@PDA5 and P-SnO_2/Fe_xO_y@PDA20 also revealed identical XRD patterns, indicating that the carbothermal reduction takes place during the heat treatment in N_2 atmosphere when PDA is present (Fig. S4). Elemental mapping images (Fig. 3j) demonstrates uniform distribution of Sn, Fe, O, C, and N elements throughout the microspheres, confirming homogeneous composition and successful PDA-derived N-doped carbon coating.

The chemical states and surface composition of the P-SnO_2/Fe_xO_y@PDA10 microspheres were systematically investigated by X-ray photoelectron spectroscopy (XPS), as summarized in Fig. 4. The survey spectrum (Fig. 4a) clearly demonstrates the presence of Sn, Fe, O, C, and N elements, confirming the successful formation of SnO_2/Fe_xO_y composites coated with N-doped carbon. The high-resolution Sn 3*d* spectrum (Fig. 4b) shows two distinct peaks at approximately 495.0 eV and 486.5 eV, corresponding to Sn $3d_{3/2}$ and Sn $3d_{5/2}$, respectively [29]. The binding energies are characteristic of Sn^{4+}, confirming that tin exists predominantly as SnO_2 in the composite. The Fe 2*p* spectrum (Fig. 4c) reveals multiple components. Peaks at 725.7 eV (Fe $2p_{1/2}$) and 712.2 eV (Fe $2p_{3/2}$) can be assigned to Fe^{3+}, while those at 723.8 eV (Fe $2p_{1/2}$) and 710.5 eV (Fe $2p_{3/2}$) are attributed to Fe^{2+} [30]. A large peak is also observed at 716.2 eV, which corresponds to the Sn $2p_{2/3}$ [31]. The O 1 *s* spectrum (Fig. 4d) can be deconvoluted into three main peaks. The peaks at 533.3 and 531.5 eV correspond to adsorbed H_2O molecules and

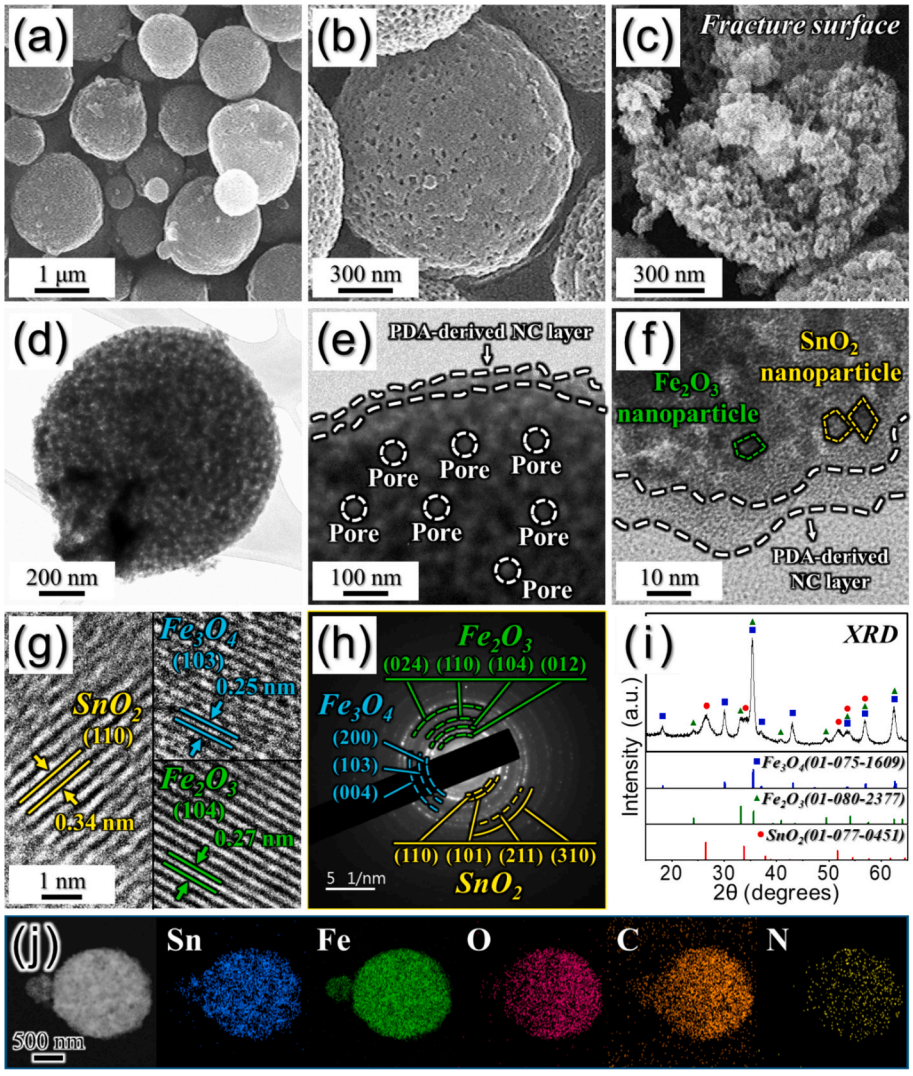

Fig. 3. Physical characterizations of P-SnO_2/Fe_xO_y@PDA10 microspheres after coating process: (a–c) FE-SEM images, (d–f) TEM images, (g) HR-TEM images, (h) SAED pattern, (i) XRD pattern, and (j) elemental mapping images.

–OH groups, respectively, while the peak at 530.0 eV is attributed to metal–oxygen bonds (Sn–O/Fe–O) [32]. This suggests the coexistence of lattice oxygen, surface hydroxyl groups, and moisture on the sample surface. The C 1 *s* spectrum (Fig. 4e) shows multiple peaks, indicating the complex carbon environment introduced by PDA-derived carbon. The main peaks at 288.0, 286.3, 285.1, and 284.3 eV are attributed to O–C=O, C–O, C–N/C–C, and C=C/C–C bonds, respectively, confirming the successful N-doping and oxygen-containing functional groups within the carbon [33–35]. The N 1 *s* spectrum (Fig. 4f) is deconvoluted into four peaks centered at 402.5, 400.5, 399.8, and 398.6 eV, which are ascribed to oxidized N, graphitic N, pyrrolic N, and pyridinic N, respectively [36,37]. The presence of multiple types of nitrogen functionalities highlights the effective incorporation of N-doped sites within the carbon layer, which is beneficial for enhancing electrical conductivity and providing active sites for electrochemical reactions. Collectively, these XPS results confirm that P-SnO_2/Fe_xO_y@PDA10 microspheres are composed of SnO_2, Fe_2O_3, and Fe_3O_4 uniformly coated with N-doped carbon, endowing the material with improved electronic conductivity and structural stability. Additionally, ICP-OES analysis (Table S2) further supports the coexistence of Sn and Fe species, revealing an atomic ratio of approximately 1:5 (Sn:Fe). As shown in Fig. S5a, the TGA curve exhibits an initial weight loss below 150 °C, which is attributed to the evaporation of physically adsorbed water. A more significant weight loss of approximately 33 wt% occurs between 200 and 500 °C, primarily due to the thermal decomposition of the N-doped carbon layer. During this temperature range, the oxidation of Fe_3O_4 to Fe_2O_3 also takes place, which involves oxygen uptake and contributes to a slight mass increase. Nevertheless, the dominant combustion of the carbon coating results in a net weight loss of 33 wt%. This aligns closely with elemental analysis, which indicates the presence of

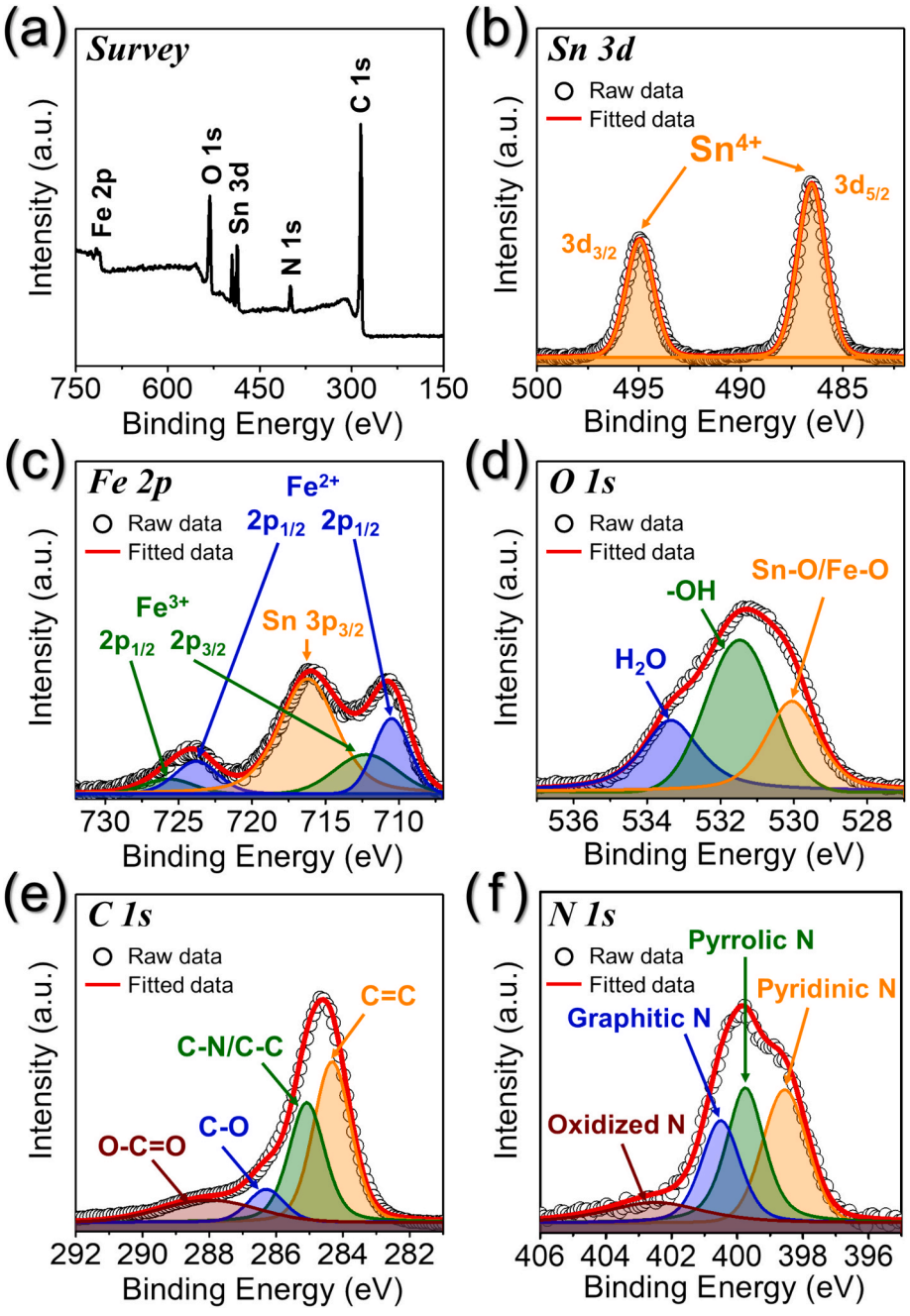

Fig. 4. (a) XPS survey spectrum, (b) Sn 3*d*, (c) Fe 2*p*, (d) O 1 *s*, (e) C 1 *s*, and (f) N 1 *s* XPS spectrum of P-SnO_2/Fe_xO_y@PDA10 microspheres.

30.1 wt% carbon and 4.4 wt% nitrogen, confirming the successful incorporation of PDA-derived N-doped carbon into the composite. Raman analysis of P-SnO_2/Fe_xO_y@PDA10 microspheres (Fig. S5b) shows the characteristic D and G bands at around 1340 and 1590 cm^{-1}, respectively, with an I_D/I_G ratio of 0.88. This value reflects the coexistence of ordered and disordered structures in the N-doped carbon coating. N_2 adsorption–desorption isotherms (Fig. S5c) reveal a BET surface area of 70 $m^2\ g^{-1}$, indicative of a high degree of porosity. The corresponding BJH pore size distribution (Fig. S5d) shows a dominant pore diameter centered at ~ 30–40 nm, which is consistent with the mesoporous nature observed in the TEM images (Fig. 3e).

To elucidate the effect of 3D porous structure, F-SnO_2/Fe_xO_y microspheres were prepared from the spray solution that does not contain PS nanobeads (Fig. S6). The microspheres exhibited non-aggregated independent microspherical morphology as can be ascertained from the FE-SEM image in Fig. S6a. From the fractured FE-SEM image and TEM image shown in Figs. S6b and c the filled interior could be identified since PS nanobeads that act as a porogen were not included inside the microspheres. Notably, lattice fringes in Fig. S6d, SAED pattern in Fig. S6e, and the XRD pattern shown in Fig. S6f altogether reveal that the microspheres are consisted of SnO_2 and Fe_2O_3, together with Fe_3O_4 phases. It is in direct contrast to P-SnO_2/Fe_2O_3 microspheres, where only SnO_2 and Fe_2O_3 phases could be identified. This phenomenon can be explained as follows: When PS nanobeads are introduced during the synthesis, a porous structure is formed, facilitating effective oxygen diffusion throughout the particle. Consequently, the oxidation of iron nitrate ($Fe(NO_3)_3$) fully progresses to Fe_2O_3. In contrast, in the absence of PS nanobeads, particles aggregate more densely, restricting oxygen penetration into the interior regions. Under these relatively oxygen-deficient conditions, partial reduction of Fe_2O_3 occurs, resulting in the additional formation of Fe_3O_4 phases. The elemental mapping images in Fig. S6g clearly reveals the homogenous distribution of Sn, Fe, and O elements in the microspheres, with the negligible amount of C and N, consistent with the TG result presented in Fig. S2c.

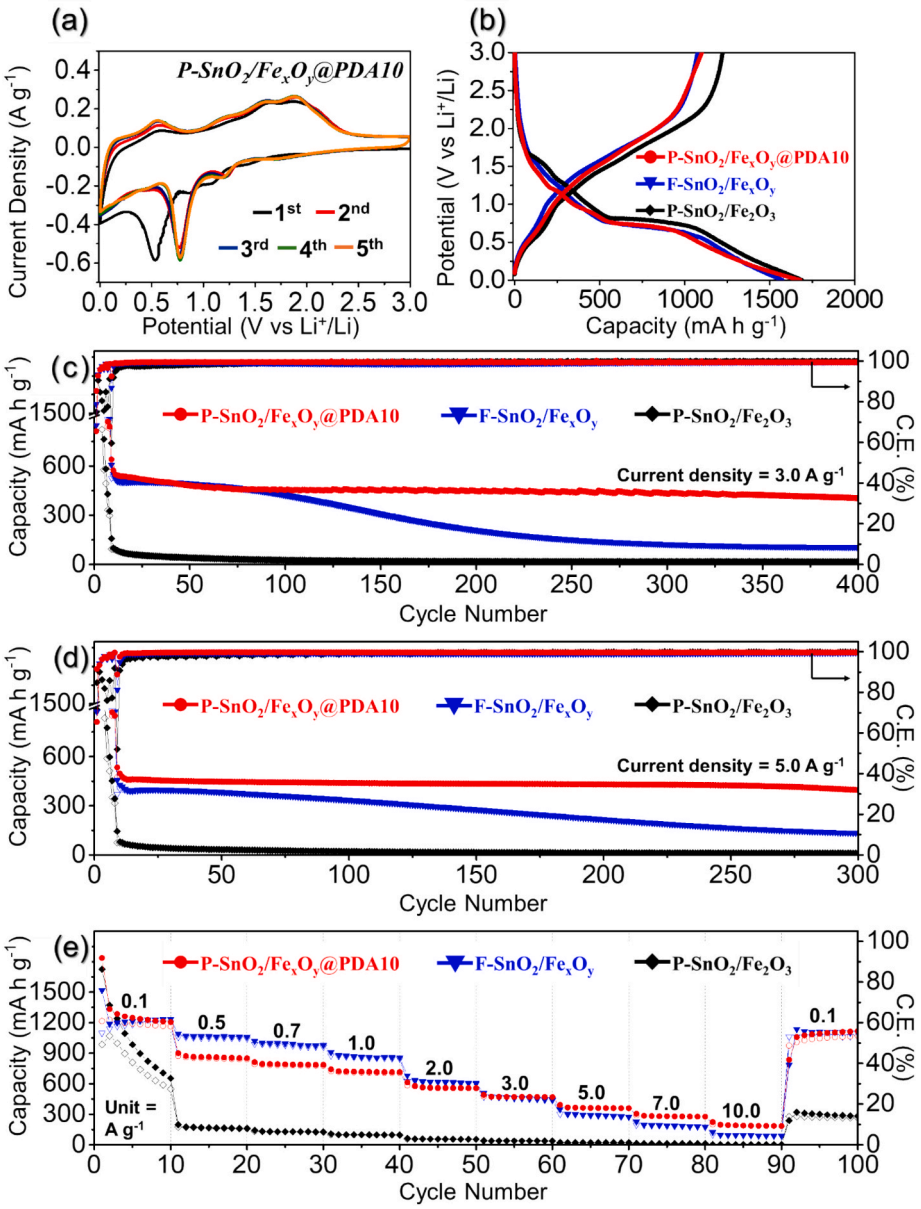

Fig. 5. Electrochemical properties of P-SnO_2/Fe_xO_y@PDA10, F-SnO_2/Fe_xO_y, and P- SnO_2/Fe_2O_3 anodes: (a) CV curves for initial five cycles of P-SnO_2/Fe_xO_y@PDA10 anode, (b) initial discharge/charge curves at a current density of 0.1 A g^{-1}, (c) cycling performance at 3.0 A g^{-1}, (d) cycling performance at 5.0 A g^{-1}, and (e) rate performance.

The electrochemical performance of P-SnO_2/Fe_xO_y@PDA10, P-SnO_2/Fe_2O_3, and F-SnO_2/Fe_xO_y microspheres as anode materials for LIBs is systematically presented in Fig. 5. Here, P-SnO_2/Fe_2O_3 and F-SnO_2/Fe_xO_y microspheres were adopted as control samples to directly examine the effect of carbon coating and 3D interconnected pores on the lithium-ion storage performance, respectively. CV measurements were performed for P-SnO_2/Fe_xO_y@PDA10, P-SnO_2/Fe_2O_3, and F-SnO_2/Fe_xO_y microspheres at a scan rate of 0.1 mV s^{-1} within the potential window of 0.001–3.0 V over the first five cycles, as depicted in Fig. 5a and S7. In the initial cathodic scan for P-SnO_2/Fe_xO_y@PDA10 microspheres, the peaks observed from ~1.1 to 0.7 V (vs. Li^+/Li) are attributed to the overlapping stepwise conversion reactions of SnO_2, Fe_2O_3, and Fe_3O_4 [38–40]. Fe_2O_3, Fe_3O_4, and SnO_2 is converted to Fe^0 and Sn^0, all accompanied by the formation of Li_2O [38–40]. The broad peak centered at ~ 0.5 V is associated with the alloying of metallic Sn with Li^+ to form Li_xSn [41]. During the initial anodic scan, distinct oxidation peaks can be observed primarily around 0.6, 1.6, and 1.8 V, corresponding to the reversible electrochemical reactions of Sn and Fe-based species [42,43]. The broad oxidation peak centered near 0.6 V is attributed to the partial oxidation of Li_xSn alloys formed during the cathodic process back to Sn [43]. The two distinct anodic peaks observed at approximately 1.6 and 1.8 V are ascribed to the successive oxidation of Fe^0 to Fe^{2+} and Fe^{2+} to Fe^{3+}, respectively [42]. It should be noted that the first CV cycle shows clear differences from the subsequent cycles. These deviations mainly originate from irreversible processes in the initial lithiation/de-lithiation, such as electrolyte decomposition with SEI formation, irreversible conversion of SnO_2 and Fe_xO_y into metallic Sn, Fe, and Li_2O, and partial trapping of Li-ion within the electrode matrix [44,45]. In this initial conversion step, the oxide particles are decomposed into ultrafine Sn and Fe nanocrystals uniformly dispersed in a Li_2O matrix, which improves the reversibility of subsequent conversion/alloying reactions and modifies the reaction kinetics [44,45]. As a result, the redox peaks in the following cycles shift to slightly different potentials, after which the CV curves stabilize with reproducible peak positions and intensities. The consistent shape and position of the anodic peaks from the 2nd to the 5th cycles indicate the good reversibility and electrochemical stability of the electrode material. Moreover, the slightly increased current intensity after the initial cycle suggests the activation of the electrode material upon cycling and the enhanced kinetics facilitated by the conductive N-doped carbon coating derived from PDA. The CV curves for P-SnO_2/Fe_2O_3 and F-SnO_2/Fe_xO_y microspheres exhibited peaks at similar potential (Fig. S7). The charge–discharge profiles of the microspheres during the initial cycle at 0.1 A g^{-1} are presented in Fig. 5b. Distinct plateaus associated with the redox reactions of Fe and Sn species were observed at similar potentials, which are consistent with the CV results. The discharge/charge capacities of P-SnO_2/Fe_xO_y@PDA10, F-SnO_2/Fe_xO_y, and P-SnO_2/Fe_2O_3 microspheres were 1679/1101, 1573/1075, 1689/1222 mA h g^{-1}, with initial Coulombic efficiencies of 65.6 %, 68.3 %, and 72.3 %, respectively. P-SnO_2/Fe_2O_3 microspheres exhibited the highest initial Coulombic efficiency (ICE) among the three, despite its relatively large specific surface area, which is generally expected to promote increased SEI formation and lower ICE. This may be attributed to the absence of Fe_3O_4 in the composite, which generally exhibits lower ICE in comparison to Fe_2O_3 counterpart, as reported in the previous reports [46,47]. The ICE of P-SnO_2/Fe_xO_y@PDA10 was the lowest, which can be attributed to the presence of the nitrogen-doped carbon coating derived from PDA. This N-doped carbon layer, while enhancing electronic conductivity and structural integrity during subsequent cycling, increases surface area and introduces more active sites for electrolyte decomposition. Consequently, this amplifies initial irreversible capacity losses associated with SEI formation, resulting in lower ICE compared to uncoated porous samples.

The long-term cycle performances of P-SnO_2/Fe_xO_y@PDA10, P-SnO_2/Fe_2O_3, and F-SnO_2/Fe_xO_y microspheres were tested at various current densities (0.5, 1.0, 3.0 and 5.0 A g^{-1}, Fig. 5c, d and S8). P-SnO_2/Fe_xO_y@PDA10 microspheres exhibited remarkable cycling stability even at high current densities, retaining capacities of 406 mA h g^{-1} after 400 cycles at 3.0 A g^{-1} and 397 mA h g^{-1} after 300 cycles at 5.0 A g^{-1}. In stark contrast, the uncoated P-SnO_2/Fe_2O_3 microspheres exhibited rapid capacity fading, attributed to structural degradation resulting from the fragile pore-wall architecture, which is susceptible to mechanical stress during repetitive lithiation/delithiation processes. Dense F-SnO_2/Fe_xO_y microspheres demonstrated intermediate stability but notably inferior capacity retention compared to P-SnO_2/Fe_xO_y@PDA10 microspheres, highlighting the critical role of N-doped carbon coating in buffering volume changes. The rate capability test (Fig. 5e) further confirms the superior performance of the N-doped carbon-coated porous microspheres. The capacity retention of P-SnO_2/Fe_xO_y@PDA10 microspheres when the current density changed from 0.1 A g^{-1} to 10.0 A g^{-1} was 15.3 %, exceeding twice the value observed for F-SnO_2/Fe_xO_y microspheres (7.1 %). The origin for the high rate capability may be attributed to the conformal N-doped carbon coating that provided 3D conductive carbonaceous matrix and porous structure that enabled the facile penetration of the electrolyte and enhanced the contact between electrode and electrolyte. P-SnO_2/Fe_2O_3 microspheres exhibited severe capacity decay at the initial few cycles, which resulted in very low capacities at higher current densities. Furthermore, to emphasize the advantages of the present material, a comparative summary of the electrochemical performance of recently reported SnO_2-, Fe_xO_y-, and SnO_2/Fe_xO_y-based anodes is provided in Table S3. As shown, the P-SnO_2/Fe_xO_y@PDA10 anode exhibits superior reversible capacity, rate capability, and long-term cycling stability compared with previously reported materials, highlighting the effectiveness of the design strategy.

To clarify the mechanism underlying the rapid Li-ion storage in P-SnO_2/Fe_xO_y@PDA10 microspheres, CV measurements were carried out for three different anodes at scan rates ranging from 0.1 to 2.0 mV s^{-1} (Fig. 6 and S9). The relationship between the peak current (i) and the scan rate (v) follows a power law ($i = av^b$), where the b-value offers insights into the charge storage mechanism—whether it is primarily governed by surface capacitive processes or by diffusion [48,49]. When the b-value approaches 1, the behavior is mainly surface-controlled, while a b-value near 0.5 points to a diffusion-limited process. By plotting log(i) against log(v) for the main redox peaks (R1, R2, O1, O2, and O3) indicated by arrows in Fig. 6a, S9a, and S9c, the b-values were extracted. For P-SnO_2/Fe_xO_y@PDA10, these b-values were determined to be 0.89, 0.60, 0.52, 0.80, and 0.81, respectively. P-SnO_2/Fe_xO_y@PDA10 higher b-values than F-SnO_2/Fe_xO_y microspheres, likely due to the N-doped carbon coating that improves the electrical conductivity and 3D porous structure which minimizes Li-ion diffusion pathways and maximizes electrode/electrolyte interface, thus promoting capacitive charge storage. Despite the intrinsic advantages of P-SnO_2/Fe_2O_3 microspheres, such as increased electrode–electrolyte contact area and shortened diffusion pathways, the b-values obtained from the CV analysis are notably lower compared to those of the filled-structure microspheres (Fig. S9b). This unexpected result can be primarily attributed to the fragile nature of the pore-wall framework, which is verified by the cycling performance. The mechanically unstable and thin pore walls in the porous structure are highly susceptible to structural collapse and pulverization during repeated charge–discharge cycles (five CV curves were obtained at each scan rates, meaning that the CV curves of the anode at sweep rate of 2.0 mV s^{-1} are collected after 25 cycles, for which P-SnO_2/Fe_2O_3 microspheres already suffered from a large capacity decay). As a result, the accessible surface area and the integrity of the electrochemically active sites are significantly compromised over cycling, which in turn reduces the overall capacitive contribution to the charge storage process. To quantitatively separate capacitive and diffusion-controlled contributions, the current at each potential was deconvoluted, allowing the relative fraction of capacitive response to be calculated using the following equation: $i = k_1\nu + k_2\nu^{1/2}$ [50,51]. The former reflects a surface-controlled charge storage mechanism, in

contrast to the latter, which represents a diffusion-limited electrochemical response. At a scan rate of 2.0 mV s^{-1}, capacitive contributions accounted for 72 %, 27 %, and 61 % of the total current in P-SnO_2/Fe_xO_y@PDA10, P-SnO_2/Fe_2O_3, and F-SnO_2/Fe_xO_y microspheres, respectively (Fig. 6c, e, and g). The evolution of capacitive behavior with increasing scan rate from 0.1 to 2.0 mV s^{-1} is shown in Fig. 6d, f, and h. P-SnO_2/Fe_xO_y@PDA10 characterized by the interconnected 3D porous matrix, which amplifies surface capacitive effects and electrode–electrolyte contact and highly conductive N-doped carbon exhibited the highest capacitive contributions.

To elucidate the differences in electrochemical behavior and structural stability among the three samples, EIS measurements and FE-SEM analyses were conducted before and after cycling (Fig. 7a–g). Nyquist plots (Fig. 7a–c) were collected for P-SnO_2/Fe_xO_y@PDA10, F-SnO_2/Fe_xO_y, and P-SnO_2/Fe_2O_3 electrodes before cycling (denoted as "Fresh"), after the 9th cycle, and after 300 cycles, which were further deconvoluted by Randles-type equivalent circuit shown in Fig. S10. Charge transfer resistance (R_{ct}) values calculated from the semicircle in the high-frequency region for the microspheres were 41, 53, and 59 Ω, respectively (Table S4) [52,53]. P-SnO_2/Fe_2O_3 exhibited a higher R_{ct} in

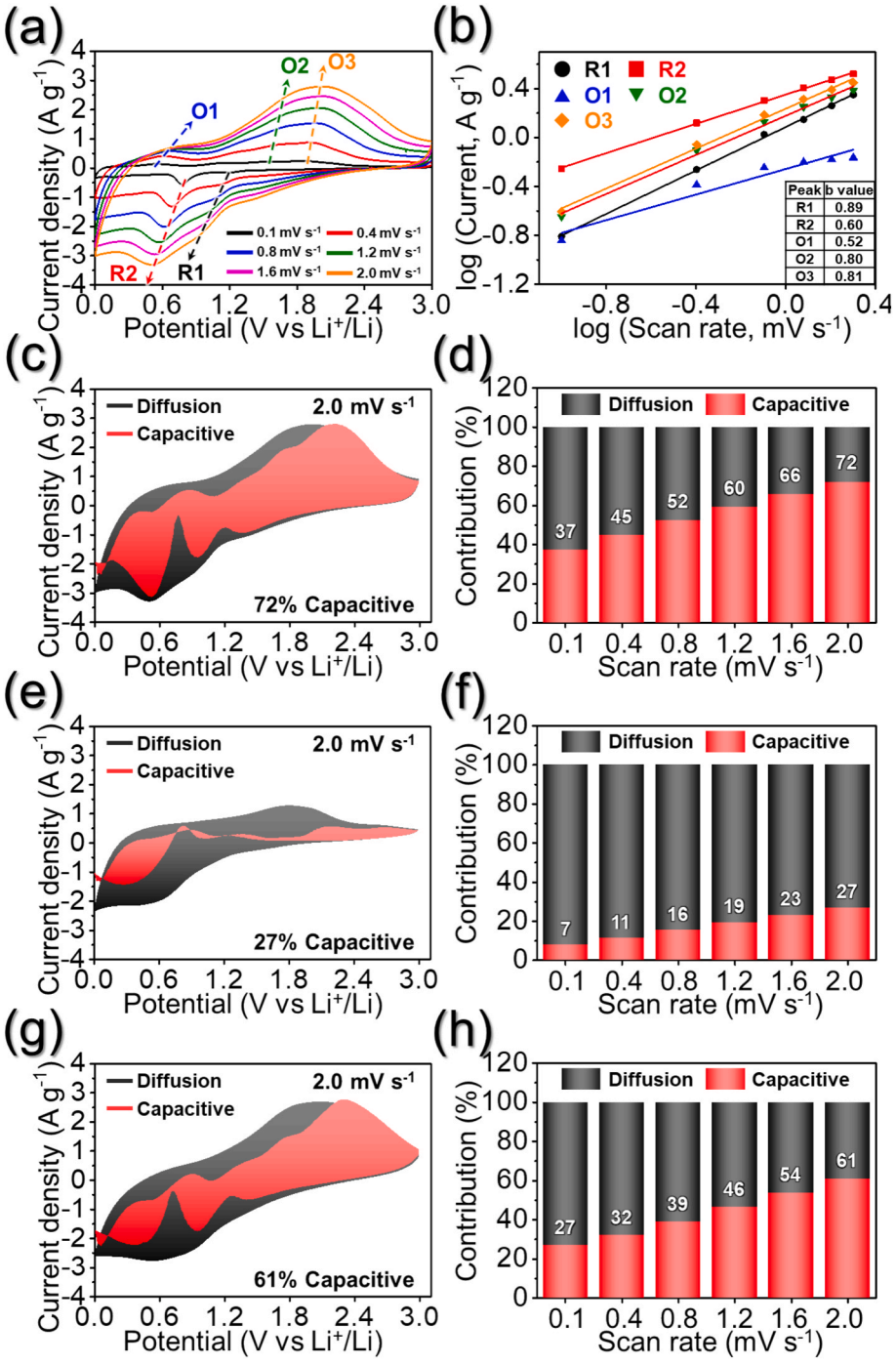

Fig. 6. Electrochemical reaction dynamics analysis of (a–d) P-SnO_2/Fe_xO_y@PDA10, (e, f) P- SnO_2/Fe_2O_3, (g, h) F-SnO_2/Fe_xO_y anodes: (a) CV curves obtained at various scan rates, (b) current response (*i*) vs. scan rate (*n*) at each redox peak, (c, e, g) CV curves with the capacitive fraction shown by the red region at a scan rate of 2.0 mV s^{-1}, and (d, f, h) bar chart showing the percentage of the capacitive contribution at different scan rates. (For interpretation of the references to colour in this figure legend, the reader is referred to the web version of this article.)

comparison to F-SnO_2/Fe_xO_y, which can be attributed to its relatively higher exposed surface area. The enhanced surface area, while beneficial for active site exposure, can also lead to an increase in interfacial charge-transfer barriers, thereby resulting in elevated R_{ct} values compared to the denser, filled microsphere counterparts. After 9 cycles (Fig. 7b), R_{ct} of P-SnO_2/Fe_xO_y@PDA10 microspheres was found to be comparable to that of F-SnO_2/Fe_xO_y microspheres, while P-SnO_2/Fe_2O_3 microspheres exhibited a relatively higher R_{ct}. This increase is presumably due to the collapse of the porous nanostructure, leading to extensive formation of the SEI and, consequently, greater interfacial resistance. Upon extended cycling (300 cycles, Fig. 7c), the disparity in impedance became more pronounced. P-SnO_2/Fe_xO_y@PDA10 microspheres still maintained a low resistance, which can be attributed to the enhanced structural robustness imparted by the N-doped carbon coating, effectively mitigating nanostructural degradation and suppressing excessive SEI formation during repetitive cycles. F-SnO_2/Fe_xO_y electrode retained better stability than the porous sample, but still suffered from a gradual increase in impedance. To further investigate the lithium-ion diffusion characteristics, the Warburg impedance (Z_w) was analyzed by plotting Z_{re} versus $\omega^{-1/2}$ (Fig. 7d). P-SnO_2/Fe_xO_y@PDA10 electrode exhibited the lowest slope, indicating the highest Li^+ diffusion coefficient among the three samples after extended cycling. FE-SEM images after 300 cycles (Fig. 7e–g) reveal the morphological evolution of each electrode. P-SnO_2/Fe_xO_y@PDA10 sample (Fig. 7e) retains its original microsphere structure with minimal cracking or fragmentation, confirming the superior mechanical stability imparted by the carbon shell. By contrast, F-SnO_2/Fe_xO_y (Fig. 7f) and especially P-SnO_2/Fe_2O_3 (Fig. 7g) show pronounced structural disintegration and collapse, with the latter exhibiting severe pulverization and loss of the spherical morphology. Collectively, these results demonstrate that the integration of a robust N-doped carbon coating on the P-SnO_2/Fe_xO_y microspheres is crucial for achieving long-term electrochemical stability and fast charge transfer kinetics. The combination of high electrical conductivity and structural resilience enables P-SnO_2/Fe_xO_y@PDA10 electrode to outperform both the dense and bare porous counterparts under high-rate and prolonged cycling conditions.

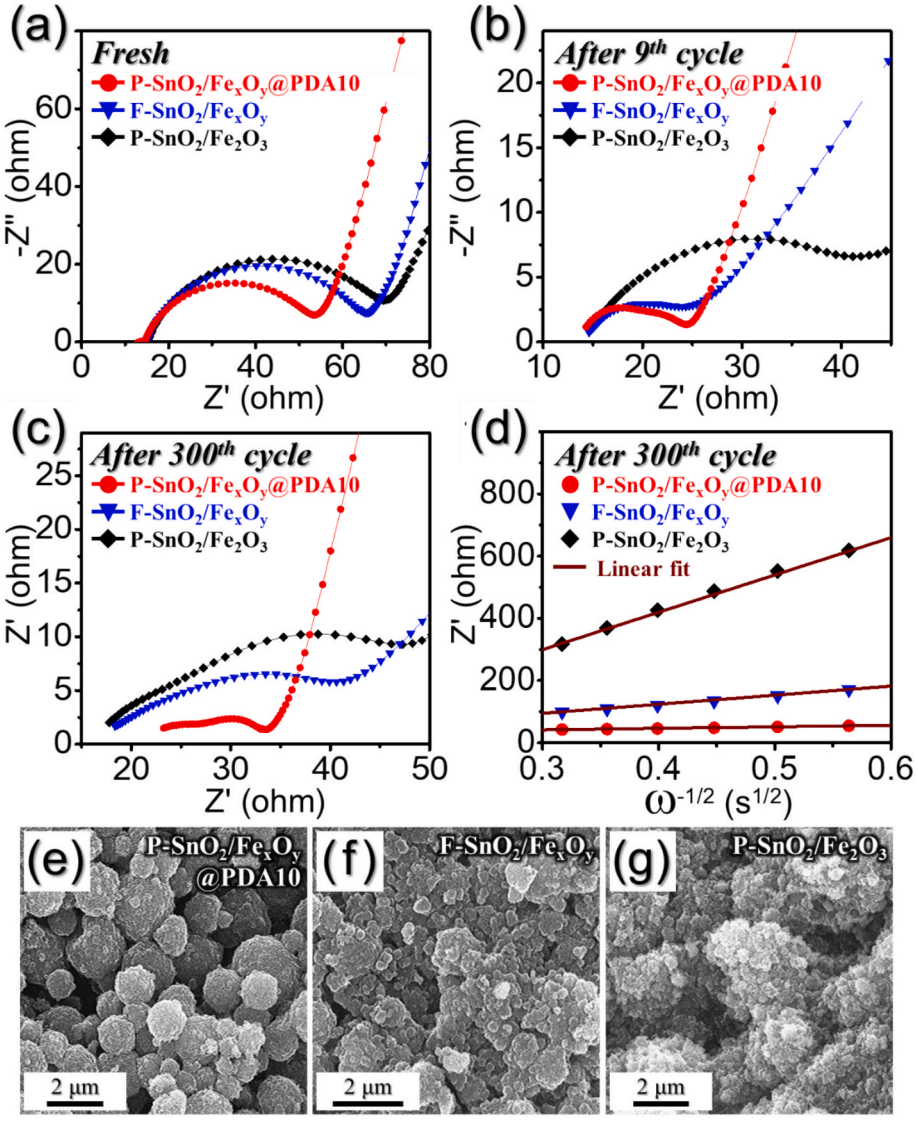

Fig. 7. (a–d) Nyquist impedance plots and (e–g) FE-SEM images of P-SnO_2/Fe_xO_y@PDA10, F-SnO_2/Fe_xO_y, and P-SnO_2/Fe_2O_3 anodes after 300th cycle: (a) before cycling, (b) after 9th cycle, (c) after 300th cycle, (d) relationships between the real part of the impedance (Z_{re}) and $\omega^{-1/2}$ obtained after 300 cycles at 3.0 A g^{-1}, (e) P-SnO_2/Fe_xO_y@PDA10, (f) F-SnO_2/Fe_xO_y, and (g) P-SnO_2/Fe_2O_3 anodes obtained after 300 cycles at 3.0 A g^{-1}.

Conclusion

In summary, we present a scalable method for synthesizing three-dimensional porous SnO_2/Fe_xO_y microspheres uniformly coated with N-doped carbon, serving as advanced anode materials for lithium-ion batteries. The unique microspheres, fabricated via spray pyrolysis using Sn-based MOF, Fe nitrate, PVP, and PS nanobeads, followed by polydopamine-derived carbonization, feature a highly interconnected porous network of ultrafine SnO_2 and Fe_xO_y nanoparticles. The abundant mesopores facilitate lithium-ion diffusion and maximize the electrode–electrolyte interface, while the conformal N-doped carbon shell enhances electronic conductivity and mechanical robustness, effectively accommodating volume changes during cycling. Electrochemical evaluations confirm that the optimized P-SnO_2/Fe_xO_y@PDA10 microspheres deliver high reversible capacity, outstanding rate performance, and excellent cycling stability, clearly outperforming both dense and uncoated porous controls. These results highlight the critical synergy between hierarchical porosity and robust carbon coating in promoting rapid charge transport and long-term structural integrity. This work provides valuable insight into the rational design of durable, high-performance anode materials and demonstrates a promising strategy for scalable production of next-generation lithium-ion battery electrodes.

CRediT authorship contribution statement

Hye Seon Ka: Writing – original draft, Validation, Software, Investigation, Conceptualization. **Geon Hui Oh:** Visualization, Validation, Methodology, Data curation. **Ji Hun Baek:** Visualization, Methodology, Investigation. **Jae Seob Lee:** Writing – original draft, Visualization, Resources. **Jin-Sung Park:** Writing – review & editing, Writing – original draft, Resources, Conceptualization. **Jung Sang Cho:** Writing – review & editing, Supervision, Project administration, Funding acquisition, Conceptualization.

Declaration of competing interest

The authors declare that they have no known competing financial interests or personal relationships that could have appeared to influence the work reported in this paper.

Acknowledgements

This work was supported by the Korea Institute of Energy Technology Evaluation and Planning (KETEP) and the Ministry of Trade, Industry & Energy (MOTIE) of the Republic of Korea (No. RS-2024-00394769). This research was supported by the Global - Learning & Academic Research Institution for Master's, PhD students, and Postdocs (G-LAMP) Program of the NRF grant funded by the Ministry of Education (No. RS-2023-00285390).

Appendix A. Supplementary material

Supplementary data to this article can be found online at https://doi.org/10.1016/j.jiec.2025.09.004.

References

[1] W. Liu, M.-S. Song, B. Kong, Y. Cui, Adv. Mater. 29 (2017) 1603436, https://doi.org/10.1002/adma.201603436.
[2] J. Xu, X. Cai, S. Cai, Y. Shao, C. Hu, S. Lu, S. Ding, Energy Environ. Mater. 6 (2023) e12450, https://doi.org/10.1002/eem2.12450.
[3] E. Feyzi, A.K. MR, X. Li, S. Deng, J. Nanda, K. Zaghib, Next Energy **5** 100176 (2024). https://doi.org/10.1016/j.nxener.2024.100176.
[4] H. Zhang, G. Meng, Q. Liu, Y. Luo, M. Niederberger, L. Feng, J. Luo, X. Liu, Small 19 (2023) e2303165, https://doi.org/10.1002/smll.202303165.
[5] C. Yuan, H.B. Wu, Y. Xie, X.W. Lou, Angew. Chem. Int. Ed. Engl. 53 (2014) 1488–1504, https://doi.org/10.1002/anie.201303971.
[6] C. Zhao, S. Yao, C. Li, Y. An, S. Zhao, X. Sun, K. Wang, X. Zhang, Y. Ma, Chem. Eng. J. 497 (2024) 154535, https://doi.org/10.1016/j.cej.2024.154535.
[7] X. Lan, X. Xiong, J. Liu, B. Yuan, R. Hu, M. Zhu, Small 18 (2022) e2201110, https://doi.org/10.1002/smll.202201110.
[8] S. Zhao, C.D. Sewell, R. Liu, S. Jia, Z. Wang, Y. He, K. Yuan, H. Jin, S. Wang, X. Liu, Z. Lin, Adv. Energy Mater. 10 (2019) 1902657, https://doi.org/10.1002/aenm.201902657.
[9] Y. Zhao, X. Li, B. Yan, D. Xiong, D. Li, S. Lawes, X. Sun, Adv. Energy Mater. 6 (2016) 1502175, https://doi.org/10.1002/aenm.201502175.
[10] A.-A.B. Abdel-Aziz, I.M. Ghayad, F. El-Taib Heakal, R.M. El Nashar, J. Electrochem. Soc. **172** 023503 (2025). https://doi.org/10.1149/1945-7111/adada4.
[11] E. Muchuweni, E.T. Mombeshora, C.M. Muiva, T.S. Sathiaraj, J. Energy Storage 73 (2023) 109013, https://doi.org/10.1016/j.est.2023.109013.
[12] Y. Yang, W. Yuan, X. Zhang, C. Wang, Y. Yuan, Y. Huang, Y. Ye, Z. Qiu, Y. Tang, Renew. Sustain. Energy Rev. 127 (2020) 109884, https://doi.org/10.1016/j.rser.2020.109884.
[13] H.B. Wu, J.S. Chen, H.H. Hng, X.W. Lou, Nanoscale 4 (2012) 2526–2542, https://doi.org/10.1039/C2NR11966H.
[14] Y. Lu, L. Yu, X.W. Lou, Chem 4 (2018) 972–996, https://doi.org/10.1016/j.chempr.2018.01.003.
[15] C.S. Kim, R. Saroha, H.H. Choi, J.H. Oh, G.D. Park, D.-W. Kang, J.S. Cho, J. Ind. Eng. Chem. 121 (2023) 489–498, https://doi.org/10.1016/j.jiec.2023.02.004.
[16] J. Ye, A.C. Baumgaertel, Y.M. Wang, J. Biener, M.M. Biener, ACS Nano 9 (2015) 2194–2202, https://doi.org/10.1021/nn505490u.
[17] Z. Liu, X. Yuan, S. Zhang, J. Wang, Q. Huang, N. Yu, Y. Zhu, L. Fu, F. Wang, Y. Chen, Y. Wu, NPG Asia Mater. 11 (2019) 12, https://doi.org/10.1038/s41427-019-0112-3.
[18] J.G. Ryu, S.J. Park, D.K. Hong, S.H. Shin, Korean J. Chem. Eng. 40 (2023) 497–503, https://doi.org/10.1007/s11814-022-1227-8.
[19] H. Chen, X. Hou, F. Chen, S. Wang, B. Wu, Q. Ru, H. Qin, Y. Xia, Carbon 130 (2018) 433–440, https://doi.org/10.1016/j.carbon.2018.01.021.
[20] J.H. Kim, B.R. Kim, J.S. Im, Korean J. Chem. Eng. 40 (2023) 2839–2846, https://doi.org/10.1007/s11814-023-1529-5.
[21] Z. Chen, X. Wu, Z. Sun, J. Pan, J. Han, Y. Wang, H. Liu, Y. Shen, J. Li, D.-L. Peng, Q. Zhang, Adv. Energy Mater. 14 (2024) 2400132, https://doi.org/10.1002/aenm.202400132.
[22] M.R.I. Rocky, V. Nulu, S.K.Y. Sohn, Korean J. Chem. Eng. 42 (2025) 1693–1704, https://doi.org/10.1007/s11814-025-00481-6.
[23] T.G. Barclay, H.M. Hegab, S.R. Clarke, M. Ginic-Markovic, Adv. Mater. Interfaces 4 (2017) 1601192, https://doi.org/10.1002/admi.201601192.
[24] H. Lee, S.M. Dellatore, W.M. Miller, P.B. Messersmith, Science 318 (2007) 426–430, https://doi.org/10.1126/science.1147241.
[25] J.-S. Park, J.K. Kim, J.H. Hong, J.S. Cho, S.-K. Park, Y.C. Kang, Nanoscale 11 (2019) 19012–19057, https://doi.org/10.1039/c9nr05575d.
[26] Y. Zhu, S.H. Choi, X. Fan, J. Shin, Z. Ma, M.R. Zachariah, J.W. Choi, C. Wang, Adv. Energy Mater. 7 (2016) 1601578, https://doi.org/10.1002/aenm.201601578.
[27] Y.-C. Xiao, C.-Y. Xu, X.-Y. Sun, Y. Pei, P.-P. Wang, F.-X. Ma, L. Zhen, Chem. Eng. J. 336 (2018) 427–435, https://doi.org/10.1016/j.cej.2017.12.021.
[28] C. Lei, F. Han, D. Li, W.-C. Li, Q. Sun, X.-Q. Zhang, A.-H. Lu, Nanoscale 5 (2013) 1168–1175, https://doi.org/10.1039/c2nr33043a.
[29] W. Xia, H. Wang, X. Zeng, J. Han, J. Zhu, M. Zhou, S. Wu, Crst. Eng. Comm. 16 (2014) 6841–6847, https://doi.org/10.1039/c4ce00884g.
[30] J. Tang, H. Qu, C. Sun, X. Xiao, H. Ji, J. Wang, J. Li, G. Ji, X. Zhang, H.-M. Cheng, G. Zhou, Adv. Mater. 37 (2025) e2420238, https://doi.org/10.1002/adma.202420238.
[31] X. Duan, J. Liu, F. Lv, T. Liu, W. Cui, J. Wang, Q. Wang, S. Yuan, J. Energy Storage 86 (2024) 111308, https://doi.org/10.1016/j.est.2024.111308.
[32] J.-S. Park, J.H. Hong, S.H. Yang, Y.C. Kang, J. Mater. Chem. A 8 (2020) 12124–12133, https://doi.org/10.1039/d0ta04305b.
[33] D.C. Marcano, D.V. Kosynkin, J.M. Baerlin, A. Sinitskii, Z. Sun, A. Slesarev, L. B. Alemany, J.M. Tour, ACS Nano 4 (2010) 4806–4814, https://doi.org/10.1021/nn1006368.
[34] J. Cheng, C. Lyu, H. Li, J. Wu, Y. Hu, B. Han, K. Wu, M. Hojamberdiev, D. Geng, Appl Catal B 327 (2023) 122470, https://doi.org/10.1016/j.apcatb.2023.122470.
[35] U.N. Maiti, J. Lim, K.E. Lee, W.J. Lee, S.O. Kim, Adv. Mater. 26 (2014) 615–619, https://doi.org/10.1002/adma.201303503.
[36] J.S. Lee, N. Kitchamsetti, J.S. Cho, Chem. Eng. J. 487 (2024) 150465, https://doi.org/10.1016/j.cej.2024.150465.
[37] J. Ge, L. Fan, J. Wang, Q. Zhang, Z. Liu, E. Zhang, Q. Liu, X. Yu, B. Lu, Adv. Energy Mater. 8 (2018) 150465, https://doi.org/10.1002/aenm.201801477.
[38] Y. Wang, Z.X. Huang, Y. Shi, J.I. Wong, M. Ding, H.Y. Yang, Sci. Rep. 5 (2015) 9164, https://doi.org/10.1038/srep09164.
[39] Q. Li, H. Li, Q. Xia, Z. Hu, Y. Zhu, S. Yan, C. Ge, Q. Zhang, X. Wang, X. Shang, S. Fan, Y. Long, L. Gu, G.-X. Miao, G. Yu, J.S. Moodera, Nat. Mater. 20 (2021) 76–83, https://doi.org/10.1038/s41563-020-0756-y.
[40] N.K. Chaudhari, M.-S. Kim, T.-S. Bae, J.-S. Yu, Electrochim. Acta 114 (2013) 60–67, https://doi.org/10.1016/j.electacta.2013.09.169.
[41] W. Zhang, Y. Liu, Z. Qin, L. Yu, L. Jiabiao, Z. Tao, Z.-H. Huang, Batteries 10 (2024) 412, https://doi.org/10.3390/batteries10120412.
[42] S. Chaudhari, M. Srinivasan, J. Mater. Chem. 22 (2012) 23049, https://doi.org/10.1039/c2jm32989a.
[43] S. Wang, G. Xu, K. Wang, B. Han, Y. Wang, L. Li, D. Ju, M. Chai, D. Zhang, W. Zhou, Curr. Res. Green Sustain. 4 (2021) 100099, https://doi.org/10.1016/j.crgsc.2021.100099.
[44] P. Poizot, S. Laruelle, S. Grugeon, L. Dupont, J.M. Tarascon, Nature 407 (2000) 496–499, https://doi.org/10.1038/35035045.

[45] K. Cao, T. Jin, L. Yang, L. Jiao, Mater. Chem. Front. 1 (2017) 2213–2242, https://doi.org/10.1039/C7QM00175D.
[46] J.-S. Xu, Y.-J. Zhu, A.C.S. Appl, Mater. Interfaces 4 (2012) 4752–4757, https://doi.org/10.1021/am301123f.
[47] C. Duan, F. Zhu, C. Wang, X. Ke, G. Ren, Y. Meng, Ionics 26 (2020) 4327–4338, https://doi.org/10.1007/s11581-020-03574-w.
[48] J. Liu, Y. Zhang, L. Zhang, F. Xie, A. Vasileff, S.-Z. Qiao, Adv. Mater. 31 (2019) e1901261, https://doi.org/10.1002/adma.201901261.
[49] G.D. Park, J.-S. Park, J.K. Kim, Y.C. Kang, Chem. Eng. J. 428 (2022) 131051, https://doi.org/10.1016/j.cej.2021.131051.
[50] T.-C. Liu, W.G. Pell, B.E. Conway, J. Electrochem. Soc. 145 (1998) 1882–1888, https://doi.org/10.1149/1.1838571.
[51] D. Su, K. Kretschmer, G. Wang, Adv. Energy Mater. 6 (2015) 1501785, https://doi.org/10.1002/aenm.201501785.
[52] Y. Zhang, H. Li, J. Liu, J. Liu, H. Ma, F. Cheng, J. Energy Chem. 63 (2021) 312–319, https://doi.org/10.1016/j.jechem.2021.07.029.
[53] F. Liu, Z. Chen, G. Fang, Z. Wang, Y. Cai, B. Tang, J. Zhou, S. Liang, Nano-Micro Lett. 11 (2019) 25, https://doi.org/10.1007/s40820-019-0256-2.